PHYSICAL REVIEW C VOLUME 50, NUMBER 5 NOVEMBER 1994

Production cross sections and the particle stability of proton-rich nuclei from ^{58}Ni fragmentation

B. Blank, S. Andriamonje, R. Del Moral, J. P. Dufour, A. Fleury, T. Josso, and M. S. Pravikoff
Centre d'Etudes Nucléaires de Bordeaux-Gradignan, F-33175 Gradignan Cedex, France
and Institut National de Physique Nucléaire et de Physique des Particules, Paris, France

S. Czajkowski, Z. Janas,* A. Piechaczek, E. Roeckl, K.-H. Schmidt, K.Sümmerer, W. Trinder, and M. Weber
Gesellschaft für Schwerionenforschung, Planckstrasse 1, D-64291 Darmstadt, Germany

T. Brohm, A. Grewe, E. Hanelt, A. Heinz, A. Junghans, C. Röhl, S. Steinhäuser, and B. Voss
Institut für Kernphysik der Technische Hochschule Darmstadt, Schlossgartenstrasse 9, D-64289 Darmstadt, Germany

M. Pfützner
Institute of Experimental Physics, University of Warsaw, PL-00-681 Warsaw, Hoża 69, Poland

(Received 27 May 1994)

Using a primary beam of ^{58}Ni at 650 MeV/nucleon impinging on a beryllium target, production cross sections of proton-rich fragments from projectile fragmentation have been measured at the projectile-fragment separator FRS at Gesellschaft für Schwerionenforschung Darmstadt m.b.H. The experimental data ranging from nickel to scandium for isotopes close to stability as well as for fragments at the proton drip line are compared to predictions of the microscopic ISApace code, to calculations with a revised abrasion-ablation model and with the statistical abrasion model, and to the results of the empirical parametrization EPAX. Besides these systematic measurements, evidence for the particle stability of ^{50}Ni has been found for the first time, whereas the nuclei ^{49}Co and ^{54}Cu are shown to be unbound. These observations are compared to mass predictions.

PACS number(s): 25.70.Mn, 25.60.+v

I. INTRODUCTION

Since the pioneering experiments at Berkeley [1,2], projectile fragmentation has been widely used in order to produce radioactive isotopes far from stability. Zero-degree spectrometers are used at GANIL [3], RIKEN [4], MSU [5], and GSI [6] together with an energy-loss technique [7] to select radioactive nuclei produced in projectile fragmentation.

The measurements of production cross sections for neutron-rich isotopes produced via projectile fragmentation [8,9] have shown that the production cross sections are strongly influenced by the N/Z ratio of the projectile ("memory effect"). Therefore projectile fragmentation of proton-rich isotopes should be a useful tool to produce exotic fragments at the proton drip line.

Usually, counting-rate estimates are based on model calculations [intranuclear-cascade (INC) + evaporation, e.g. [10,11], or abrasion ablation, e.g. [12]] or on the empirical EPAX formula [13]. Close to stability, these production rates are in reasonable agreement with the predictions, although deviations by factors of 2–5 occur. The relatively high primary-beam intensities now available at GSI and the high transmission efficiency of the projectile-fragment separator FRS [6] allow for the first time the experimental mapping of production cross sections close to the proton drip line. At lower incident energies, only production rates can be given which are linked to the low transmission of the spectrometers used yielding a high uncertainty of the transmission.

Section II of the present paper gives details of the experimental procedure, whereas Sec. III describes the analysis of the data. In Sec. IV, our results are compared to different model calculations. In Sec. V, we discuss the identification of new isotopes and the limits of stability. Section VI contains some concluding remarks.

II. EXPERIMENTAL SETUP

A primary beam of ^{58}Ni with an intensity of about 5×10^7 particles per second accelerated by the SIS synchrotron at GSI, Darmstadt, to an energy of 650A MeV impinged on a ^{9}Be target (4 g/cm^2) at the entrance of the projectile-fragment separator FRS [6]. Eight different settings of the fragment separator have been used in order to select ^{56}Ni, ^{53}Fe, ^{52}Fe, ^{50}Fe, ^{49}Fe, ^{48}Fe, ^{47}Fe, and ^{46}Fe. Because of a degrader thickness of only 1.5 g/cm^2 of aluminum, fragments between copper and scandium are transmitted through the FRS simultaneously and can be detected at the exit.

---

*On leave of absence from Institute of Experimental Physics, University of Warsaw, PL-00-681 Warsaw, Hoża 69, Poland.

0556-2813/94/50(5)/2398(10)/$06.00

Figure 1 shows a schematic drawing of the experimental setup. The secondary electron transmission monitor SEETRAM [14] was used to determine the primary-beam intensity impinging on the production target. This detector has been calibrated before the experiment with a scintillation detector at low counting rates ($< 10^4$ s^{-1}). In the intermediate focal plane after the first dipole stage, the fragments pass the wedge-shaped degrader and a position-sensitive plastic scintillator [15]. This detector permits one to deduce the magnetic rigidity of the fragments and serves as a start detector for the time-of-flight (TOF) measurement. At the exit of the FRS, a second position-sensitive plastic scintillator is used to determine the position of the fragments as well as to give a stop signal for the TOF measurement. Behind this detector, an ionization chamber MUSIC [16] measured the energy loss of the fragments in order to extract their nuclear charge.

III. ANALYSIS PROCEDURE AND RESULTS

A. Identification of the transmitted isotopes

Figure 2 shows a typical ΔE-TOF spectrum for the setting to select ^{47}Fe as well as the other $T_z = -\frac{5}{2}$ nuclei between nickel and scandium. In this spectrum, the measured TOF values have been corrected for the different flight-path lengths of the ions with different magnetic rigidity. The matrix of the different charges Z and masses A is clearly visible. For the odd-Z nuclei, we have reached the proton drip line with this setting. The "holes" in the matrix corresponding to the unbound nuclei ^{45}Mn and ^{41,42}V [17] help to unambiguously identify the different isotopes. The stability of ^{49}Co will be discussed later in this paper, so that we do not use it for identification purposes. The identification of the different isotopes is supported by model calculations [18] which predict the separation properties of the FRS.

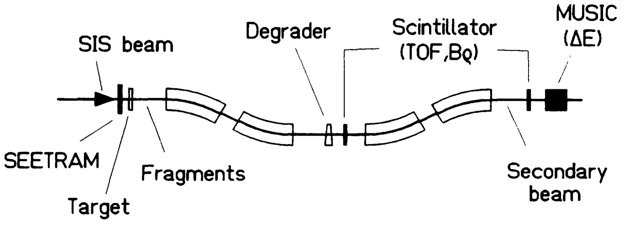

FIG. 1. Experimental setup used in the present experiment. The primary-beam intensity was measured with the SEETRAM detector in front of the target. Two position-sensitive plastic scintillators in the intermediate focal plane and at the exit of the separator served to determine the magnetic rigidity ($B\rho$) and the time of flight (TOF) for the different fragments. Their nuclear charge was determined by means of their energy loss (ΔE) in the MUSIC detector.

B. Corrections of the counting rate

The counting rates of the different isotopes obtained from the two-dimensional spectra as shown in Fig. 2 have to be corrected for transmission losses in the spectrometer, for losses due to secondary interactions in the target and in the intermediate degrader as well as in the detectors, for the dead time of the data acquisition, and for the detector efficiencies.

The dead time is determined in the usual way via two scalars. One scalar is triggered by all events independent from the data acquisition, whereas the second one is triggered only when the event is registered by the data acquisition. The dead time determined in such a way varies for the different runs between 60% for the settings selecting isotopes close to stability and 10% for those far from stability.

Transmission losses are taken into account by using ion optical-model calculations with the code LIESCHEN [18,19]. The relativistic energy of the fragments results in high transmission values for the selected isospin series between 50% for titanium and close to 100% for nickel. The neighboring isospin rows are still character-

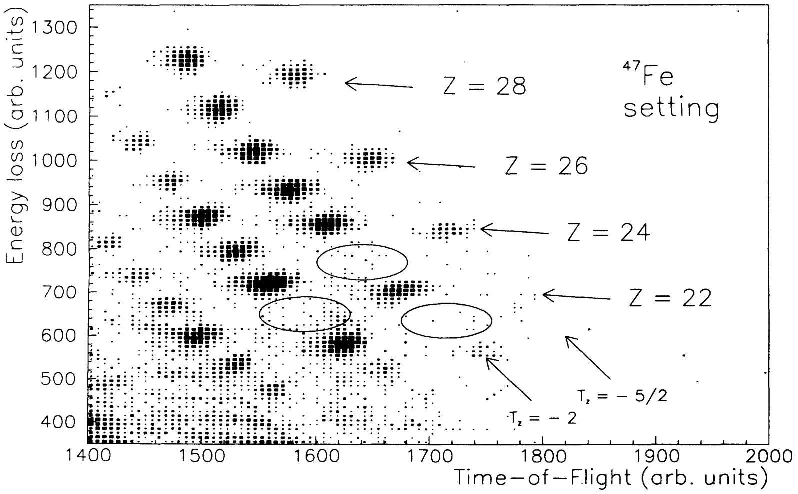

FIG. 2. Two-dimensional plot of the energy loss of the fragments in the MUSIC detector versus their time of flight between the intermediate focal plane and the exit of the FRS. The data were obtained with the FRS being optimized for transmitting ^{47}Fe. The "holes" corresponding to unbound nuclei at the proton drip line (^{45}Mn, ^{41,42}V) can be used to identify the different isotopes. The arrows indicate the rows of constant nuclear charge Z and constant isospin projection T_z.

ized by a transmission of about 10%–20%. However, detailed measurements of the velocity distribution of projectile fragments from ^{86}Kr [20] as well as from ^{129}Xe [21] fragmentation showed that the velocity shift of the center of the fragment distribution depends not only on the mass loss as assumed by Morrissey [22] and as used in the simulation, but also on the isospin projection of the final fragment. This finding may affect the calculated transmissions, especially if low transmissions are involved. However, as the experimental information on this effect is still scarce, we used the mass-loss-dependent shift of Morrissey [22] in the calculations, keeping in mind that our analysis may thus slightly under- or overestimate the production cross sections depending on the velocity shift.

The losses due to secondary interactions are calculated in the following way [19]. The number of fragments observed, N_f, is related to the production cross section σ_f and to the number of projectiles, N_p, via the formula

$$N_f = N_p \sigma_f \frac{N_A}{A_t} d_t f_1 f_2 \,.$$

A_t is the atomic mass of the target, N_A is Avogadro's constant, and d_t is the target thickness. The factor f_1 corrects for the losses in the production target, whereas the factor f_2 corrects for losses in the degrader.

The correction factor f_1 reads as follows:

$$f_1 = \frac{\exp(-\mu_{pt} d_t) - \exp(-\mu_{ft} d_t)}{d_t(\mu_{ft} - \mu_{pt})} \,,$$

where $\mu_{it} = (N_A/A_t)\sigma^t_{it}$. The total interaction cross sections σ^t for the projectile in the target (index pt) as well as for the fragment in the target (index ft) are calculated by means of a semiempirical parametrization for the total interaction cross sections [23,24].

The correction in the degrader can be calculated in the following way:

$$f_2 = \exp(-\mu_{fd} d_d) \,.$$

In this case, μ_{fd} is determined with the total interaction cross section σ^t_{fd} of the fragment in the degrader of thickness d_d: $\mu_{fd} = (N_A/A_d)\sigma^t_{fd}$. Because of the large target and degrader thicknesses, this correction amounts to about 20%.

C. Experimental results

The resulting production cross sections σ_f for fragments between nickel and scandium are given in Table I. Several isotopes have been measured with different settings of the fragment separator FRS. For these nuclei, cross sections have been calculated as the error-weighted average value. However, in order to avoid too high uncertainties due to the calculated transmissions, we have taken into account only cross sections for nuclei with transmissions higher than 10% for a given setting.

D. Errors of the cross sections

The errors of the cross sections given in Table I merit a detailed description. The errors for the primary-beam intensity are due to the calibration constant of the SEETRAM detector. This constant is determined, as described above, with a scintillator at a low counting rate. The error of this constant is of the order of 5%.

The error of the corrections of the secondary interactions in target and degrader is directly dependent on the error of the total-reaction cross-section formula. The authors of [24] give an overall uncertainty of 10% for their parametrization. The uncertainties of the thicknesses of target and degrader are much smaller than the uncertainty of the total reaction cross section; therefore, the error due to the target and degrader thickness uncertainty is not taken into account.

The number of fragments observed depends on the efficiency of the detectors used. The different isotopes are identified by a ΔE-TOF-$B\rho$ method. With its four independent ionization chambers, the efficiency of the MUSIC detector is 100%. The time of flight is determined by two independent measurements on the left-hand side and on the right-hand side of the scintillators at the intermediate and the final focal plane. Because of this redundant information, the TOF efficiency is 100%. The $B\rho$ determination relies on the position determination with the scintillator at the exit of the FRS. For this correction, no redundant information from other detectors is available, which slightly reduces the $B\rho$ efficiency to values between 95% and 98%.

Besides the statistical errors of the counting rates for the most exotic isotopes, the transmission calculations have the highest uncertainty. The calculations for a recent experiment [8] have been compared to experimentally deduced transmissions based on the longitudinal momentum distribution. As mentioned above, this comparison yielded systematic discrepancies between experimental transmissions and those calculated [20]. In our analysis, we used an error of 20% for transmission higher than 20%, increasing to 50% for a transmission of 10%.

The errors estimated in such a way are then used to modify the number of incident particles, N_p, and the number of observed fragments, N_f, respectively. With these figures, we calculate new production cross sections. The differences between these values and the central values are finally added quadratically. This procedure yields the asymmetric error bars given in Table I.

IV. DISCUSSION OF THE EXPERIMENTAL RESULTS

A. Comparison with calculations

In Fig. 3, the experimental results are compared to different calculations. For these comparisons, we use

TABLE I. Experimentally determined production cross sections for the fragmentation of a ^{58}Ni primary beam in a beryllium target. The average beam energy in the center of the target was 585 MeV/nucleon.

Isotope	Cross section (mb)		Isotope	Cross section (mb)	
^{50}Ni	0.61×10^{-7}	$+0.33\times10^{-7}$ -0.30×10^{-7}	^{51}Mn	0.10×10^{2}	$+0.28\times10^{1}$ -0.14×10^{1}
^{51}Ni	0.22×10^{-5}	$+0.67\times10^{-6}$ -0.44×10^{-6}	^{52}Mn	0.26×10^{2}	$+0.21\times10^{2}$ -0.86×10^{1}
^{52}Ni	0.32×10^{-4}	$+0.93\times10^{-5}$ -0.52×10^{-5}	^{43}Cr	0.17×10^{-5}	$+0.39\times10^{-6}$ -0.29×10^{-6}
^{53}Ni	0.93×10^{-3}	$+0.26\times10^{-3}$ -0.12×10^{-3}	^{44}Cr	0.21×10^{-4}	$+0.46\times10^{-5}$ -0.34×10^{-5}
^{54}Ni	0.12×10^{-1}	$+0.31\times10^{-2}$ -0.15×10^{-2}	^{45}Cr	0.92×10^{-3}	$+0.20\times10^{-3}$ -0.14×10^{-3}
^{55}Ni	0.31×10^{0}	$+0.13\times10^{0}$ -0.78×10^{-1}	^{46}Cr	0.13×10^{-1}	$+0.30\times10^{-2}$ -0.21×10^{-2}
^{56}Ni	0.42×10^{1}	$+0.86\times10^{0}$ -0.41×10^{0}	^{47}Cr	0.29×10^{0}	$+0.12\times10^{0}$ -0.74×10^{-1}
^{57}Ni	0.45×10^{2}	$+0.93\times10^{1}$ -0.51×10^{1}	^{48}Cr	0.20×10^{1}	$+0.42\times10^{0}$ -0.30×10^{0}
^{50}Co	0.22×10^{-4}	$+0.61\times10^{-5}$ -0.35×10^{-5}	^{49}Cr	0.10×10^{2}	$+0.29\times10^{1}$ -0.20×10^{1}
^{51}Co	0.39×10^{-3}	$+0.10\times10^{-3}$ -0.53×10^{-4}	^{50}Cr	0.26×10^{2}	$+0.33\times10^{2}$ -0.10×10^{2}
^{52}Co	0.92×10^{-2}	$+0.23\times10^{-2}$ -0.11×10^{-2}	^{43}V	0.27×10^{-3}	$+0.60\times10^{-4}$ -0.43×10^{-4}
^{53}Co	0.17×10^{0}	$+0.68\times10^{-1}$ -0.43×10^{-1}	^{44}V	0.10×10^{-1}	$+0.23\times10^{-2}$ -0.16×10^{-2}
^{54}Co	0.18×10^{1}	$+0.38\times10^{0}$ -0.18×10^{0}	^{45}V	0.15×10^{0}	$+0.58\times10^{-1}$ -0.37×10^{-1}
^{55}Co	0.16×10^{2}	$+0.41\times10^{1}$ -0.20×10^{1}	^{46}V	0.15×10^{1}	$+0.34\times10^{0}$ -0.24×10^{0}
^{56}Co	0.29×10^{2}	$+0.94\times10^{1}$ -0.66×10^{1}	^{47}V	0.86×10^{1}	$+0.26\times10^{1}$ -0.17×10^{1}
^{46}Fe	0.12×10^{-6}	$+0.53\times10^{-7}$ -0.46×10^{-7}	^{48}V	0.22×10^{2}	$+0.47\times10^{2}$ -0.94×10^{1}
^{47}Fe	0.25×10^{-5}	$+0.61\times10^{-6}$ -0.44×10^{-6}	^{39}Ti	0.60×10^{-6}	$+0.15\times10^{-6}$ -0.12×10^{-6}
^{48}Fe	0.26×10^{-4}	$+0.62\times10^{-5}$ -0.39×10^{-5}	^{40}Ti	0.65×10^{-5}	$+0.15\times10^{-5}$ -0.11×10^{-5}
^{49}Fe	0.77×10^{-3}	$+0.18\times10^{-3}$ -0.11×10^{-3}	^{41}Ti	0.41×10^{-3}	$+0.92\times10^{-4}$ -0.65×10^{-4}
^{50}Fe	0.11×10^{-1}	$+0.26\times10^{-2}$ -0.14×10^{-2}	^{42}Ti	0.59×10^{-2}	$+0.13\times10^{-2}$ -0.92×10^{-3}
^{51}Fe	0.32×10^{0}	$+0.22\times10^{0}$ -0.10×10^{0}	^{43}Ti	0.22×10^{0}	$+0.78\times10^{-1}$ -0.52×10^{-1}
^{52}Fe	0.21×10^{1}	$+0.44\times10^{0}$ -0.21×10^{0}	^{44}Ti	0.17×10^{1}	$+0.38\times10^{0}$ -0.27×10^{0}
^{53}Fe	0.13×10^{2}	$+0.35\times10^{1}$ -0.17×10^{1}	^{45}Ti	0.92×10^{1}	$+0.29\times10^{1}$ -0.17×10^{1}
^{54}Fe	0.31×10^{2}	$+0.16\times10^{2}$ -0.88×10^{1}	^{46}Ti	0.23×10^{2}	$+0.12\times10^{3}$ -0.11×10^{2}
^{46}Mn	0.21×10^{-4}	$+0.46\times10^{-5}$ -0.33×10^{-5}	^{40}Sc	0.53×10^{-2}	$+0.22\times10^{-2}$ -0.12×10^{-2}
^{47}Mn	0.38×10^{-3}	$+0.91\times10^{-4}$ -0.64×10^{-4}	^{41}Sc	0.48×10^{-1}	$+0.18\times10^{-1}$ -0.12×10^{-1}
^{48}Mn	0.10×10^{-1}	$+0.25\times10^{-2}$ -0.15×10^{-2}	^{42}Sc	0.50×10^{0}	$+0.13\times10^{0}$ -0.88×10^{-1}
^{49}Mn	0.18×10^{0}	$+0.94\times10^{-1}$ -0.51×10^{-1}	^{43}Sc	0.68×10^{1}	$+0.21\times10^{1}$ -0.11×10^{1}
^{50}Mn	0.15×10^{1}	$+0.31\times10^{0}$ -0.18×10^{0}	^{44}Sc	0.16×10^{2}	$+0.83\times10^{3}$ -0.83×10^{1}

a revised version of the geometrical abrasion-ablation model [12], the recently developed statistical abrasion model [25], the ISApace code [26], and the empirical parametrization EPAX [13].

The two abrasion-ablation models are conceptually different in the description of nuclear abrasion: The geometrical model [12] assumes the nuclei to be spheres with sharp surfaces from which the geometrical overlap is abraded. The statistical abrasion [25] considers them as agglomerations of quasifree nucleons described by diffuse density distributions, from which nucleons are abraded when they undergo a nucleon-nucleon collision. The INC model [10] is also based on the nucleon-nucleon picture, but follows the history of the individual nucleons throughout the nuclear collision in detail. So, contrary to the abrasion-ablation models, multiple nucleon-nucleon interactions as well as excitations of the nucleons are taken into account by the INC model.

The geometrical abrasion and the statistical abrasion as well as the INC model are followed by an evaporation code. We used an average excitation energy of 27 MeV per abraded nucleon [27] for the abrasion models, which is in agreement with the excitation energy as determined by the INC code. The gradually increasing complexity of these model descriptions may allow us to identify the essential physics of the fragmentation process when they are compared to the data.

All three models are in good agreement with the data for the isotopes close to stability which are produced with relatively high cross sections (see Fig. 3). For more neutron-deficient fragments, the comparison is hampered by the limited range of the model calculations, which, as a result of computation statistics, are restricted to cross sections larger than about 1 μb. Nevertheless, discrepancies show up, e.g., for the neutron-deficient nickel isotopes, where the geometrical abrasion apparently predicts too high cross sections. This failure can originate either from the abrasion process, i.e., from an overesti-

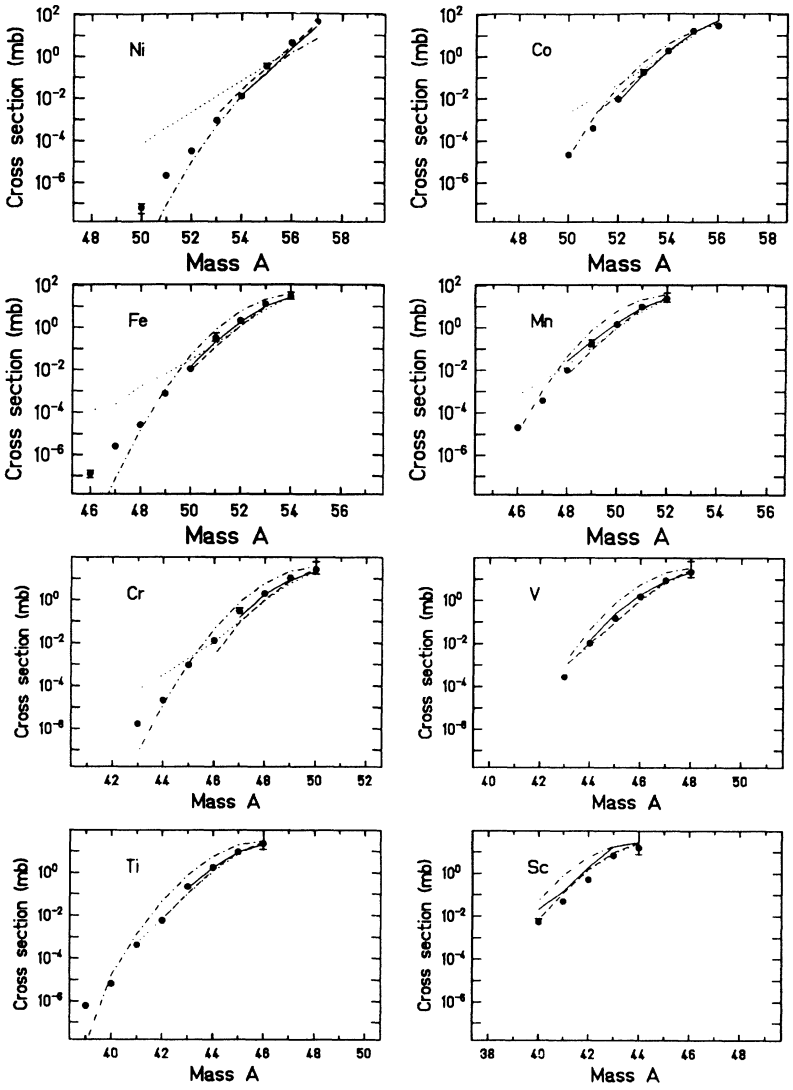

FIG. 3. Experimental production cross sections for fragments produced with a ^{58}Ni primary beam at 650 MeV/nucleon in a beryllium target. These cross sections (solid circles) are compared to theoretical predictions based on the ISApace code (solid line), to the statistical-abrasion model (dashed line), a modified version of the abrasion-ablation model (dotted line), and to the empirical EPAX formula (dash-dotted line).

mated width of the prefragment distribution, or from the ablation stage, i.e., an underestimation of proton evaporation. Since the statistical abrasion model uses the same excitation energy and the same evaporation calculation but nicely reproduces the slope, the disagreement must be attributed to the abrasion stage. As discussed in [25], the statistical abrasion model determines the width of the prefragment isotopic distributions from the nucleon-nucleon collision statistics. This yields narrower distributions than the hypergeometrical approach of the geometrical abrasion formalism, where an uncorrelated removal of neutrons and protons is assumed [12]. Note that the prefragment charge dispersion in the statistical abrasion model should be close to the one obtained from an INC calculation and that this is confirmed by the observation that the ISApace code also reproduces the falloff of the cross sections for neutron-deficient isotopes. Furthermore, we state that the overestimation of the cross sections by the geometrical abrasion model becomes less severe for fragments far from the projectile, e.g., the titanium and scandium isotopes. This is in line with the well-known argument that such fragment distributions are not sensitive to the abrasion stage, but are dominated by the evaporation process. The present data, in particular the cross sections for the nickel isotopes, therefore allow one to conclude on the longstanding discussion concerning the origin of the prefragment charge dispersion [12,25]. For the first time, we can discriminate between the hypergeometrical approach, which yields too wide prefragment isotopic distributions, and the statistical description, whose results are consistent with experimental data. The statistical abrasion model as well as the INC calculation include this realistic description of the prefragment charge dispersion.

Concerning the practical problem of estimating cross sections for fragments close to the proton drip line, it can be stated that none of the reaction models predicts cross sections below the μb level. In this range, the EPAX formula [13] is actually the only reliable source of prediction. It yields a remarkable agreement for the whole body of measured data. A closer look shows, however, that the Gaussian-shaped decrease of the production cross sections on the proton-rich side assumed by the EPAX formula predicts too high cross sections close to stability, whereas it significantly underestimates the production rates near the proton drip line. For ^{47}Fe, the discrepancy already reaches more than a factor of 35, whereas it amounts to about a factor of 750 for ^{46}Fe. As more and more cross-section measurements are now available, it is foreseen to use the whole body of fragmentation data to adjust the parameters of this practical formula in order to precisely predict production cross sections at the proton drip line.

B. Slope of the isotope distribution on the proton-rich side

The fact that the production cross sections fall off more slowly than predicted by the EPAX formula when approaching the proton drip line is in agreement with an observation from a recent GANIL experiment [17] where only about a factor of 20 was found between the production rates of ^{47}Fe and ^{46}Fe.

In order to obtain an estimate of the production cross sections at the drip line, the measured data have been fitted with a purely exponential slope. The cross sections decrease by a factor of 20 per mass unit for a given nuclear charge Z. The fact that the decrease of the cross sections on the proton-rich side can be described by an exponential slope, whereas on the neutron-rich side a power function with a slope parameter of 1.5 is necessary [13], is not so surprising. The emission of a proton is hindered by the Coulomb barrier, which is not the case for neutrons on the neutron-rich side.

The cross-section systematics obtained in this experiment allow one to extrapolate to expected counting rates of yet-unobserved nuclei if their half-lives are long enough. A nucleus which recently attracted the attention of different groups of experimentalists as well as theoreticians is ^{45}Fe. It seems to be a very interesting nucleus, as it would be a $T_z = -\frac{7}{2}$ isotope. Although not observed in the GANIL experiment [17], it is, as a result of calculations based on mass predictions [28,29], not only a possible candidate for the direct $2p$ decay [30] but also for $\beta 1p$, $\beta 2p$, $\beta 3p$, $\beta 4p$, and even $\beta 5p$ decays. A $\beta p\alpha$ decay seems to be possible, too. With a primary-beam intensity of 10^9 s^{-1} available at GSI for ^{58}Ni in the near future, about 20 ^{45}Fe ions per day are expected to be available at the exit of the FRS, which should allow one to determine whether this isotope exists and maybe even to investigate its principal decay modes.

C. Odd-even effects in the production cross sections

Besides the exponential slope of the production cross sections in Fig. 3, one finds a significant odd-even effect in our data. Although the effect is more visible for the even-Z elements where more isotopes are bound, the odd-even staggering is also present in the odd-Z elements. For all elements, the production rate is enhanced for isotopes with odd-neutron numbers.

In order to investigate the odd-even effect also for constant neutron number, Fig. 4 shows the production cross sections for isotopes with neutron numbers $N = 21, 22, 23, 24$. In these spectra, the odd-even effect is reversed; i.e., the production rates are higher for even-Z isotopes.

We discuss the even-odd structure observed in the fragment production rates along the ideas given in Ref. [12]. There is a complex influence of pairing correlations on the ablation stage of the fragmentation reaction because both the nuclear binding energies and the level densities are modulated by neutron and proton pairing structure. For the neutron-deficient nuclei considered here, the proton separation energy plays an important role by defining the energy window in which the excited levels of a nucleus

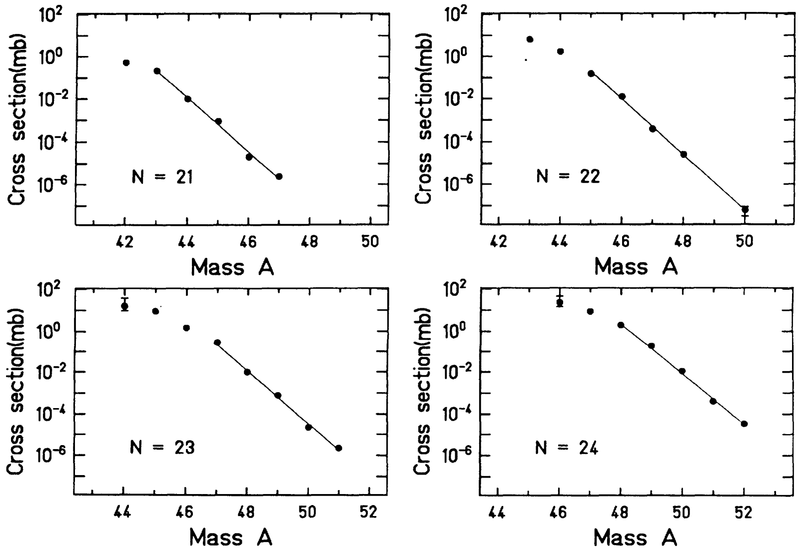

FIG. 4. Experimental production cross sections as a function of the mass number A for isotones with $N = 21, 22, 23, 24$. The experimental cross sections (solid circles) with $T_z < 0$ are fitted with an exponential function (solid line). This fit evidences the odd-even effect present in our data.

are particle bound (or unbound but more quickly deexcited by γ emission). It is expected that the production cross sections are modulated by the number of particle-bound states because they represent the end points of the individual particle evaporation cascades.

For nuclei with a constant nuclear charge Z, any even-odd structure is caused by the neutron pairing. While the energy window of particle-bound levels, determined by the proton separation energy, varies smoothly with N, the number of particle-stable levels is higher for odd-N isotopes with their higher level densities than for even-N isotopes. This explains the higher production rates for odd-N nuclei in the isotopic chains.

For constant neutron number N, the proton separation energies of even-Z nuclei are systematically higher by about 2.0–2.5 MeV than those of the neighboring odd-Z nuclei. In spite of the lower level density of even-Z isotones, this results in a larger number of particle-stable levels for even-Z isotones, which explains the observed higher production rates for even-Z nuclei in isotonic chains.

V. NEW ISOTOPES AND THE LIMITS OF STABILITY

The tuning of the FRS for ^{46}Fe permits the transmission not only to ^{46}Fe, but also to the other $T_z = -3$ isotopes with a high transmission of about 90%. Therefore this setting gives the possibility to identify the yet-unobserved isotopes ^{50}Ni and ^{42}Cr, which are predicted to be bound against one-proton emission. In order to unambiguously identify the isotopes of interest, we determined their positions at the intermediate as well as at the final focal plane, their energy loss, and their time of flight by using model calculations [18]. These calculations have been checked and slightly scaled on the basis of data obtained with the results from the setting for ^{47}Fe where we have enough of a counting rate to identify all isotopes without any doubt.

In such a way, we can predict the centroids of the position, ΔE, and TOF distributions of ^{46}Fe. We have accepted events within 3 standard deviations around these centroids; this choice enhances the background, but ensures an efficiency close to 100% for the isotopes of interest.

The same procedure has been applied to the setting for ^{47}Fe to investigate whether ^{49}Co is unbound and to the setting for ^{48}Fe in order to search for ^{54}Cu.

A. Background counting rate

For the setting of ^{46}Fe, the resulting mass spectra for the different elements identified according to their energy loss in the MUSIC detector, their TOF, and their position in the FRS focal plane are shown in Fig. 5. The copper spectrum [Fig. 5(a)] shows one count between mass units 51 and 52. The lightest copper isotope known up to now is ^{55}Cu (see also below), and lighter copper isotopes are most probably unbound [29,31]. As copper isotopes with mass numbers $A \leq 58$ are most probably produced by charge-exchange reactions induced by the ^{58}Ni beam in the ^{9}Be target, they are produced with production cross sections and parallel-momentum distributions similar to projectile fragments. Therefore the copper spectrum gives direct information concerning the background for elements close to the primary beam.

Another background information can be deduced from the cobalt spectrum [Fig. 5(c)]. As the last bound isotope is ^{50}Co (see below), it is evident from this spectrum that background counts are scattered all over the range of isotopes accepted by the separator. The spectrum of the manganese isotopes [Fig. 5(e)] may serve as an additional background check. It has been shown in the GANIL experiment [17] that ^{46}Mn is the lightest bound manganese isotope.

In general, because of the fact that the odd-Z isotopes with isospin projections $T_z < -2.5$ are unbound, the odd-Z spectra in Fig. 5 show that the background increases slowly with decreasing atomic number. This background is interpreted to result from charge-changing interactions in the matter layers at the exit of the FRS. These reactions lead to a wrong identification in the charge spectrum, whereas all the other event parameters stay unchanged and represent the main part of the contaminants.

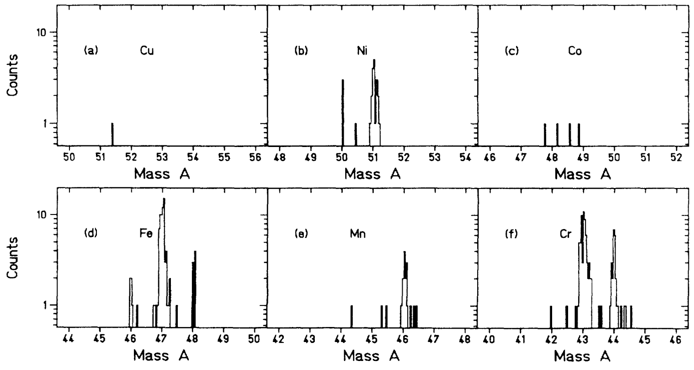

FIG. 5. Counts observed for different isotopes of elements from copper to chromium. The spectra have been obtained by setting the FRS to select ^{46}Fe.

Therefore we can conclude that close to the projectile the background is at most in the order of one count per mass unit. More generally, these background counts are scattered all over the accepted mass range.

B. Particle stability of ^{50}Ni

The number of counts for nickel isotopes in the setting for ^{46}Fe is shown in Fig. 5(b). For the yet-unobserved isotope ^{50}Ni, we find three counts which fulfill the conditions we impose on the TOF, on the energy loss, and on the position at the final focus. The count between mass numbers 50 and 51 is likely to be a background count. As the probability of having three background counts which fulfill the above-mentioned conditions and which fit very well in the mass-identification spectrum is very low, we deduce that we have found for the first time evidence for this isotope to be particle stable. In addition, the counting rate agrees with the trends of our cross-section measurements (see Fig. 4): An extrapolation of the counts observed for ^{51}Ni on the basis of our cross-section systematics yields an expected number of about four to five counts. The particle stability of ^{50}Ni is predicted by all mass formulas with proton separation energies for ^{50}Ni of about 2.5 MeV and two-proton separation energies of about 0.6 MeV (see Table II).

C. Particle instability of ^{49}Co

Since we have observed 20 counts of ^{51}Ni when setting the FRS for ^{46}Fe and 77 counts of ^{47}Fe [see Figs. 5(b) and 5(d)], we can deduce that^{49}Co is unbound, because about the same number of events is expected as for its $T_z = -\frac{5}{2}$ neighbors ^{51}Ni and ^{47}Fe. This conclusion is supported by the results obtained from the FRS setting for ^{47}Fe [Fig. 6(a)]. With this setting, ^{49}Co is expected to have a transmission close to 100%, whereas the transmission of ^{50}Co is only about 13% according to our model calculations. As the counting rate for ^{50}Co is 657 counts [Fig. 6(a)], we would expect about 250 counts for ^{49}Co, which takes into account a factor of 20 for the lower production cross section expected from the exponential A dependence shown in Fig. 4. However, in the spectrum displayed in Fig. 6(a), we find at the position expected for ^{49}Co only a very few counts at the background level. Therefore we deduce that ^{49}Co is unbound and its half-life for proton emission is short compared to the flight time through the spectrometer of about 300 ns. The same conclusion can be drawn from the counting rate of ^{51}Ni (284 counts) and ^{47}Fe (285 counts) in the same FRS setting. As these isotopes have the same isospin projection as ^{49}Co, the counting rate would be approximately the same. Assuming an upper experimental limit of one observed count, we can deduce an upper limit of the half-life of about 35 ns. ^{49}Co is predicted to be unbound by about 1.0 MeV. The mass predictions from different models are given in Table II together with the half-lives from one-proton barrier-penetration calculations using a Wood-Saxon nuclear potential and an angular momentum $l = 0$.

Although we did not observe any count for ^{48}Co beyond the background limit, we cannot decide whether it is bound, because the expected counting rate, if bound, is as low as the one for ^{46}Fe [Fig. 5(d)] or ^{50}Ni [Fig. 5(b)].

D. Particle instability of ^{54}Cu

With the FRS setting for ^{48}Fe, ^{54}Cu is expected to have a transmission close to 100%, whereas the transmission of ^{55}Cu is only about 11%. The isotope ^{55}Cu is clearly visible in the spectrum shown in Fig. 6(b). According to systematics of charge-exchange reactions [32], one would expect about a factor of 20 less counting rate for ^{54}Cu than for ^{55}Cu. Together with the higher transmission for ^{54}Cu, this should lead to a decrease of the counting rate by about a factor of 2. Therefore we expect about 15 counts for ^{54}Cu. Comparing these expected 15 counts to a maximum of one experimental count, we can state that ^{54}Cu is unbound. In fact, according to mass predictions, ^{54}Cu is unbound by 0.7 MeV (see Table II). If one assumes that the upper experimental limit is one count, we can determine an upper experimental limit of 75 ns for the half-life of ^{54}Cu.

E. Nonobservation of ^{42}Cr

The chromium spectrum [Fig. 5(f)] shows no evidence for the stability of ^{42}Cr. According to mass predictions

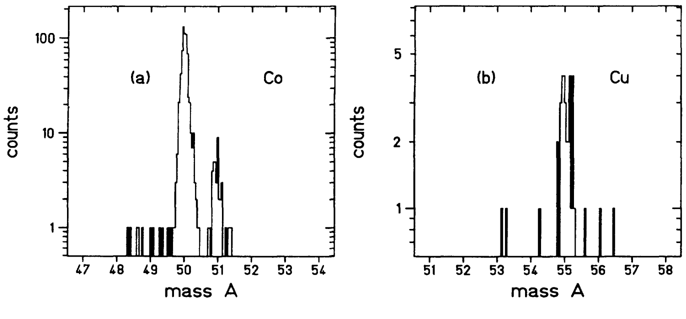

FIG. 6. (a) Number of counts of the cobalt isotopes observed in the FRS setting for ^{47}Fe. (b) Same for the copper isotopes in the FRS setting for ^{48}Fe.

TABLE II. Mass excesses Δm, one-proton separation energies S_p, two-proton separation energies S_{2p}, and barrier penetration half-lives $T_{1/2}$ for s-wave emission for different proton-rich isotopes. All energy values are in MeV, the half-lives in seconds. All models predict the stability of ^{50}Ni as well as the instability of ^{54}Cu and ^{49}Co. Mass-excess values from [28,29] are used.

	Audi and Wapstra [29]	Pape *et al.* [28]	Jänecke *et al.* [28]	Comay *et al.* [28]
^{50}Ni				
Δm	−3.79	−3.61	−4.21	−4.26
S_p	1.20	1.53	1.30	1.31
S_{2p}	0.26	0.53	0.81	0.66
^{54}Cu				
Δm	−21.96	−21.62	−21.82	−21.91
S_p	−0.40	−0.71	−0.62	−0.69
S_{2p}	1.96	1.95	2.14	2.26
$T_{1/2}$	3×10^{-9}	6×10^{-14}	6×10^{-13}	1×10^{-13}
^{49}Co				
Δm	−9.88	−9.37	−10.20	−10.24
S_p	−0.94	−1.00	−0.49	−0.65
S_{2p}	−2.20	−1.73	−2.18	−1.96
$T_{1/2}$	2×10^{-16}	8×10^{-17}	4×10^{-12}	4×10^{-14}

[28,29], this isotope may be a candidate for the direct two-proton emission [30] with a rather long half-life. The expected counting rate in our experiment is of the same order as for ^{46}Fe and ^{50}Ni. Hence we cannot draw any conclusion on the particle stability of ^{42}Cr at present.

VI. CONCLUSION

In our experiment, we have measured production cross sections for fragments produced via ^{58}Ni fragmentation in a beryllium target at an incident energy of 650 MeV/nucleon. These systematic measurements reach the proton drip line for the odd-Z nuclei and yield the first experimental data on production cross sections at the proton drip line in this mass region.

The comparison to model calculations shows that the results obtained with the ISApace code [10,11] and with the statistical abrasion model [25] reproduce the experimental results in the region where calculations are possible. The EPAX parametrization [13] yields a good overall agreement with the data as a result of the Gaussian slope for the production cross sections on the proton-rich side; however, it underestimates the production rates at the limits of stability and has to be reconsidered. A purely exponential slope seems to be more appropriate.

The FRS settings for exotic nuclei allowed us to identify the new isotope ^{50}Ni, whereas the isotopes ^{54}Cu and ^{49}Co are found to be unbound. Therefore the proton drip line for copper is reached with ^{55}Cu. As the expected counting rate for ^{48}Co and ^{42}Cr was too low, we cannot decide whether these isotopes are particle stable.

ACKNOWLEDGMENTS

We acknowledge the technical support of K.-H. Behr, A. Brünle, and K. Burkard in the preparation phase and during the experiment. H. Folger and the GSI target laboratory prepared the target and degrader layers with the necessary precision. Furthermore, we would like to acknowledge the efforts of the SIS operation crew for delivering a primary beam with high quality. We would like to express our sincere gratitude to M. Fauerbach for performing part of the ISApace calculations. One of the authors (Z.J.) would like to acknowledge support from the Alexander von Humboldt Foundation. This work has been supported by the GSI Hochschulprogramm, the German Bundesminister für Forschung und Technologie under Contract No. 06 DA 461, and the German-French collaboration program of IN$_2$P$_3$ and GSI.

---

[1] T.J.M. Symons, Y.P. Viyogi, G.D. Westfall, P. Doll, D.E. Greiner, H. Faraggi, P.J. Lindstrom, D.K. Scott, H.J. Crawford, and C. McParland, Phys. Rev. Lett. **42**, 40 (1979).

[2] G.D. Westfall, T.J.M. Symons, D.E. Greiner, H.H. Heckmann, P.J. Lindstrom, J. Mahoney, A.C. Shotter, D.K. Scott, H.J. Crawford, C. McFarlane, T.C. Awes, C.K. Gelbke, and J.M. Kidd, Phys. Rev. Lett. **43**, 1859 (1979).

[3] R. Anne, D. Bazin, A.C. Mueller, J.C. Jacmart, and M. Langevin, Nucl. Instrum. Methods A **257**, 215 (1987).

[4] M. Ishihara, Nucl. Phys. **A538**, 309c (1992).

[5] B.M. Sherill, W. Benenson, D. Mikolas, D.J. Morrissey, J.A. Nolen, Jr., and J.A. Winger, in *Proceedings of the 1st International Conference on Radioactive Nuclear Beams*, Berkeley, 1989, edited by W.D. Myers, J.M. Nitschke, and E.B. Norman (World Scientific, Singapore, 1990), p. 72.

[6] H. Geissel, P. Armbruster, K.H. Behr, A. Brünle, K. Burkard, M. Chen, H. Folger, B. Franczak, H. Keller, O. Klepper, B. Langenbeck, F. Nickel, E. Pfeng, M. Pfützner, E. Roeckl, K. Rykaczewsky, I. Schall, D. Schardt, C. Scheidenberger, K.-H. Schmidt, A. Schröter, T. Schwab, K. Sümmerer, M. Weber, G. Münzenberg, T. Brohm, H.-G. Clerc, M. Fauerbach, J.-J. Gaimard, A. Grewe, E. Hanelt, B. Knödler, M. Steiner, B. Voss, J. Weckenmann, C. Ziegler, A. Magel, H. Wollnik, J.P. Dufour, Y. Fujita, D.J. Vieira, and B. Sherrill, Nucl. Instrum. Methods B **70**, 286 (1992).

[7] J.-P. Dufour, R. Del Moral, H. Emmermann, F. Hubert, A. Fleury, D. Jean, C. Poinot, M.S. Pravikoff, H. Delagrange, and K.-H. Schmidt, Nucl. Instrum. Methods A **248**, 267 (1986).

[8] M. Weber, C. Donzaud, J.P. Dufour, H. Geissel, A. Grewe, D. Guillemaud-Mueller, H. Keller, M. Lewitowicz, A. Magel, A.C. Mueller, G. Münzenberg, F. Nickel, M. Pfützner, A. Piechaczek, M. Pravikoff, E. Roeckl, K. Rykaczewski, M.G. Saint-Laurent, I. Schall, C. Stéphan, K. Sümmerer, L. Tassan-Got, D.J. Vieira, and B. Voss, Z. Phys. A **343**, 67 (1992).

[9] J. Friese, H.-J. Körner, J. Reinhold, R. Schneider, H. Trieb, K. Zeitelhack, B. Blank, T. Brohm, Y. Fujita, H. Geissel, W. König, G. Münzenberg, F. Nickel, M. Pfützner, K. Rykaczweski, I. Schall, D. Schardt, A. Schröter, M. Steiner, K. Sümmerer, B. Voss, and J. Weckenmann, Nucl. Phys. **A553**, 753c (1993).

[10] Y. Yariv and Z. Fraenkel, Phys. Rev. C **20**, 2227 (1979).

[11] A. Gavron, Phys. Rev. C **21**, 230 (1980).

[12] J.-J. Gaimard and K.-H. Schmidt, Nucl. Phys. **A531**, 709 (1991).

[13] K. Sümmerer, W. Brüchle, D.J. Morrissey, M. Schädel, B. Szweryn, and Y. Weifan, Phys. Rev. C **42**, 2546 (1990).

[14] C. Ziegler, T. Brohm, H.-G. Clerc, H. Geissel, K.-H. Schmidt, K. Sümmerer, D.J. Vieira, and B. Voss, GSI Scientific Report No. GSI-91-1, 1990, p. 291.

[15] B. Voss, H.-G. Clerc, E. Hanelt, H. Stelzer, B. Blank, J.-J. Gaimard, H. Geissel, G. Münzenberg, K.-H. Schmidt, and K. Sümmerer, GSI Scientific Report No. GSI-89-1, 1988, p. 283.

[16] M. Pfützner, H. Geissel, G. Münzenberg, F. Nickel, Ch. Schneidenberger, K.-H. Schmidt, K. Sümmerer, T. Brohm, B. Voss, and H. Bichsel, Nucl. Instrum. Methods B **86**, 213 (1994).

[17] V. Borrell, R. Anne, D. Bazin, C. Borea, G.C. Chubarian, R. Del Moral, C. Détraz, S. Dogny, J.P. Dufour, L. Faux, A. Fleury, L.K. Fifield, D. Guillemaud-Mueller, F. Hubert, E. Kashy, M. Lewitowicz, C. Marchand, A.C. Mueller, F. Pougheon, M.S. Pravikoff, M.G. Saint-Laurent, O. Sorlin, Z. Phys. A **344**, 135 (1992).

[18] E. Hanelt and K.-H. Schmidt, Nucl. Instrum. Methods A **321**, 434 (1992).

[19] K.-H. Schmidt, E. Hanelt, H. Geissel, G. Münzenherg, and J.P. Dufour, Nucl. Instrum. Methods A **260**, 287 (1987).

[20] M. Weber, C. Donzaud, J.P. Dufour, H. Geissel, A. Grewe, D. Guillemaud-Mueller, H. Keller, M. Lewitowicz, A. Magel, A.C. Mueller, G. Münzenberg, F. Nickel, M. Pfützner, A. Piechaczek, M. Pravikoff, E. Roeckl, K. Rykaczewski, M.G. Saint-Laurent, I. Schall, C. Stéphan, K. Sümmerer, L. Tassan-Got, D.J. Vieira, and B. Voss, Nucl. Phys. A (submitted).

[21] J. Friese, H.J. Körner, J. Reinhold, R. Schneider, K. Zeitelhack, H. Geissel, A. Magel, G. Münzenberg, and K. Sümmerer, in *Proceedings of the 3rd International Conference on Radioactive Nuclear Beams*, East Lansing, Michigan, 1993, edited by D.J. Morrissey (Editions Frontières, Gif-sur-Yvette, 1993), p. 333.

[22] D.J. Morrissey, Phys. Rev. C **39**, 460 (1989).

[23] Shen Wen-qinq, Feng Jun, Zhan Wen-long, Zhu Yong-tai, and Feng En-pu, Nucl. Phys. **A491**, 130 (1989).

[24] S. Kox, A. Gamp, C. Perrin, J. Arvieux, R. Bertholet, J.F. Bruandet, M. Buenerd, R. Cherkaoui, A.J. Cole, Y. El-Masri, N. Longequeue, J. Menet, F. Merchez, and J.B. Viano, Phys. Rev. C **35**, 1678 (1987).

[25] T. Brohm and K.-H. Schmidt, Nucl. Phys. **A569**, 821 (1994).

[26] M. Fauerbach (private communication).

[27] K.-H. Schmidt, T. Brohm, H.-G. Clerc, M. Dormik, M. Fauerbach, H. Geissel, A. Grewe, E. Hanelt, A. Junghans, A. Magel, W. Morawek, G. Münzenberg, F. Nickel, M. Pfützner, C. Scheidenberger, K. Sümmerer, D. Vieira, B. Voss, and C. Ziegler, Phys. Lett. B **300**, 313 (1993).

[28] P.E. Haustein (editor), At. Data Nucl. Data Tables **39**, 185 (1988).

[29] G. Audi and A.H. Wapstra, Nucl. Phys. **A565**, 1 (1993).

[30] B.A. Brown, Phys. Rev. C **43**, R1513 (1991).

[31] F. Pougheon, J.C. Jacmart, E. Quiniou, R. Anne, D. Bazin, V. Borrel, J. Galin, D. Guerreau, D. Guillemaud-Mueller, A.C. Mueller, E. Roeckl, M.G. Saint-Laurent, and C. Détraz, Z. Phys. A **327**, 17 (1987).

[32] K. Sümmerer, M. Weber, C. Douzaud, M. Fauerbach, H. Geissel, A. Grewe, H. Keller, M. Lewitowicz, A. Magel, A.C. Mueller, G. Münzenberg, F. Nickel, M. Pfützner, A. Piechaczek, E. Roeckl, K. Rykaczewski, M.G. Saint-Laurent, I. Schall, W. Schwab, C. Stéphan, L. Tassan-Got, and B. Voss, in *Proceedings of the 3rd International Conference on Radioactive Nuclear Beams* [21], p. 425.